IET Journals
The Institution of Engineering and Technology

Adaptive backstepping approach for dc-side controllers of Z-source inverters in grid-tied PV system applications

ISSN 1751-8644
doi: 0000000000
www.ietdl.org

Phuong Vu[1], *Quan Nguyen*[2], *Minh Tran*[1], *Grazia Todeschini*[3], *Surya Santoso*[2]

[1] *School of Electrical Engineering, Hanoi University of Science and Technology, Hanoi, Vietnam*
[2] *Department of Electrical and Computer Engineering, The University of Texas at Austin, Texas, U.S.A*
[3] *College of Engineering, Swansea University, UK*
** E-mail: phuong.vuhoang@hust.edu.vn, quan.nguyenhuy@utexas.edu, minh.trantrong@hust.edu.vn, grazia.todeschini@swansea.ac.uk, ssantoso@mail.utexas.edu*

Abstract: Z-source inverters (ZSIs) are single-stage power converters with both voltage buck and boost capabilities provided by the unique impedance network and the ability to operate during shoot-through states. This study proposes a novel non-linear adaptive backstepping method for dc-side controllers in a multi-loop control scheme of the ZSI in grid-tied photovoltaic (PV) systems. Despite the variability of the capacitor and inductor values in the ZSI impedance network, the proposed controller guarantees robust and stable operation under varying levels of PV irradiance and temperature. The shoot-through duty ratio of the ZSI is obtained directly from the output of an MPPT algorithm and the measured PV and inductor currents. This strategy overcomes the disadvantages of the conventional approach such as the non-minimum phase at the dc side of the ZSI. It also eliminates the need to linearise the voltage/current characteristics of the PV arrays and ZSI model. The ac-side controllers consist of an outer proportionalâĂŞintegral voltage controller and an inner deadbeat current controller to achieve unity power factor and stable capacitor voltage in spite of grid voltage fluctuations. The efficacy of the proposed adaptive backstepping controller and the multi-loop control scheme is validated by offline and hardware-in-the-loop real-time simulations.

1 Introduction

The rapid increase of photovoltaic (PV) penetration in distribution systems necessitates a proper topology for power electronics inverters. In spite of their distinct advantages, traditional voltage-source and current-source inverters suffer from unavoidable drawbacks such as the limited ac output voltage range by the dc input voltage and the vulnerability to electromagnetic interference (EMI) [1]. The latter may cause switching-device misgating, which may result in shoot-through states and destroy the circuit.

The Z-source inverter (ZSI), which is classified as an impedance-source inverter, was first proposed in [2]. The ZSI is suitable for applications in grid-tied PV systems, taking into account the wide operating range of the input dc voltage [1, 3–7]. The ZSI is a single-stage power converter with both voltage buck and boost capabilities. This special characteristic results from the application of a unique symmetric impedance network with inductors and capacitors connected in an X-shape. With the impedance network, the ZSI can use the shoot-through state to boost the output ac voltage to a higher value than the input dc voltage, which cannot be achieved in conventional inverters [1, 2, 8]. Furthermore, the ability to handle the shoot-through state makes ZSI more reliable than the conventional inverters. Dead-time is also not required for the ZSI, which reduces the harmonic content in the output waveforms.

Fig. 1a shows the conventional multi-loop control scheme consisting of dc-side and ac-side controllers for the ZSI applications in grid-tied PV systems [1, 4, 6, 9–12]. At the dc side, PI controllers compute the shoot-through duty ratio d_{sh} to regulate the input dc voltage u_{inv} of the inverter H-bridge. This voltage control can be either direct through the peak value $\hat{u}_{inv}$ or indirect through the voltage u_C across the capacitors C_1 and C_2 in the impedance network. The latter is preferred in practical applications since it does not require complicated sensing and scaling circuits [9, 10, 13]. At the ac side, the maximum power point tracking (MPPT) block and its associated controller regulate the output voltage u_{pv} of the PV arrays and generate the reference current i^* for the ac-current loop. This ac-current loop only consists of a PI controller designed in the synchronously rotating frame. As a result, the voltage u_C across

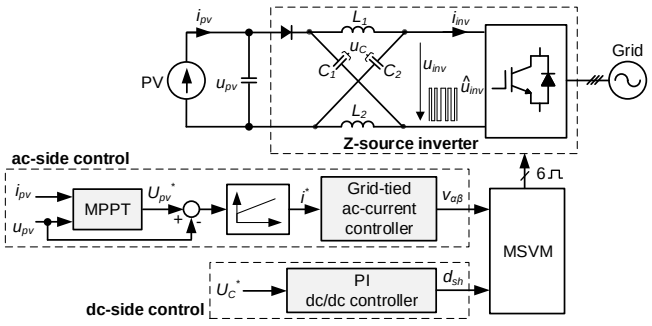

(a) The conventional control scheme.

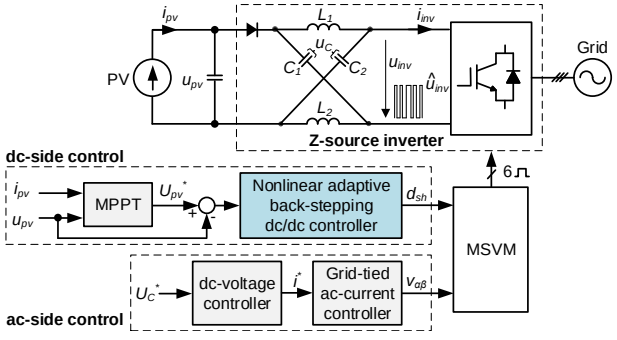

(b) The reconfigured control scheme.

Fig. 1: Circuit configuration and control schemes for the ZSI in grid-tied PV systems.

capacitors C_1 and C_2 in the conventional control scheme may be unstable in transient states of ac grids, such as voltage sag or swell.

The controllers at the dc side in Fig. 1a have non-minimum phase characteristics, i.e. the initial response opposes the direction of the change from the set-point value [1, 9–11]. The non-minimum phase characteristic results from the right half-plane zero in the transfer function of the Z-source impedance network, which cannot be completely eliminated by adjusting the values of capacitors C_1 and C_2 and inductors L_1 and L_2 [14, 15]. The non-minimum phase characteristic results in significant overshoot and undershoot in the voltage u_C when the input voltage u_{pv} of the PV arrays changes, as shown in [9, 14]. This behavior increases the harmonic distortion of the output voltage and current. Many studies have tried to resolve the negative effects of the non-minimum phase characteristic. Closed-loop PI control methods based on the linearisation of the voltage/current characteristics of PV arrays and the ZSI model have been proposed in [1, 3**?** , 4]. However, the parameters of the designed PI regulators rely heavily on the selected operating point of the dc side of the ZSI; consequently, the voltage u_C across capacitors C_1 and C_2 may experience unacceptable instability in a normal operating range of the PV arrays [11]. Other solutions to minimize the effects of the non-minimum phase consist in implementing sliding-mode control [5, 15, 16], fuzzy control [7], and neural network control [17] at the dc side. However, these approaches require the value of the equivalent load current i_{inv} of the Z-source impedance network during the shoot-through state, which is difficult to identify exactly due to harmonic distortion. In spite of the fast dynamic response, the applications of these nonlinear control approaches are also impeded by the complex control algorithms .

Considering these limitations related to the multi-loop topology and the dc-side control, the contribution of this paper is a novel dc-side control design based on the adaptive backstepping approach in a reconfigured multi-loop control scheme.

Fig. 1b shows the reconfigured control scheme. Compared to the conventional control scheme shown in Fig. 1a, the MPPT block is switched to the dc-side controllers, while the ac-side controllers are responsible for regulating the voltages u_C across the capacitors in the impedance network. With this configuration, the control at the dc side regulates the output impedance of the PV system to obtain maximum output power. This control strategy overcomes the disadvantages of the previous methods by reducing overshoot and undershoot in u_C during transient states of the ac grid while still inheriting the existing double-loop voltage-current control at the ac side of conventional grid-tied inverters.

Regarding the dc side, the proposed adaptive backstepping controller inherits the fast dynamic response from the nonlinear control approach. In addition, the controller is designed without the need to linearise the voltage/current characteristic of PV arrays and the ZSI model. The mathematical model of the proposed dc-side controller using the backstepping method also takes into account the uncertainty of the parameters in the impendance network. This uncertainty may be caused by manufacturing processes, inductance variation due to high current flow, or capacitance variation due to temperature fluctuation. Therefore, the proposed control scheme guarantees effective and robust operations even when the parameters of Z-source impedance are unknown or when the operating point of PV arrays changes under variable temperature and irradiance conditions. Unlike the conventional PI controller approach, the system global stability, which is important for any PV systems, can be mathematically proved by using the Lyapunov theory with the proposed adaptive backstepping method.

In the remainder of this paper, Section II shows a dynamic model of three-phase ZSI in grid-tied PV systems. Section III presents the proposed adaptive backstepping controller at the dc side. Off-line simulations and hardware-in-the-loop (HIL) real-time simulations are discussed in Section IV to validate the proposed control method.

2 Dynamic Modeling

The three-phase ZSI in grid-tied PV systems are a combination of a Z-network connected to a PV system and a conventional H-bridge inverter connected to an ac grid. In order to obtain the mathematical model of the system, the following assumptions are made:

- The three-phase ac-grid voltage is balanced.
- The parasitic resistances of the Z-source impedance network are ignored. The Z-source impedance network is symmetrical. This assumption will be removed later on.
- The IGBTs are ideal switches.
- In the non-shoot-through state, the dc bus voltage is constant over each switching cycle.

2.1 dc-side model

Fig. 2 shows the equivalent circuit of the ZSI at the dc side and the simplified models during the shoot-through and non-shoot-through states [2]. Since the impedance network is assumed to be symmetrical, the steady-state values of current flowing through inductors L_1 and L_2 as well as the voltages across capacitors C_1 and C_2 are identical. From Fig. 2, the low-frequency mathematical model of the Z-network using the average method is obtained as follows [4]:

$$\begin{aligned} L\frac{di_L}{dt} &= (2d_{sh}-1)u_C + (1-d_{sh})u_{pv}, \\ C\frac{du_C}{dt} &= (1-2d_{sh})i_L + (d_{sh}-1)i_{inv}, \\ C_{pv}\frac{du_{pv}}{dt} &= i_{pv} - i_L, \end{aligned} \tag{1}$$

where $d_{sh} = T_{sh}/T_s$ is the shoot-through duty ratio and T_{sh} is the shoot-through interval over a switching cycle T_s; u_C and i_L are the capacitor voltage and the inductor current in the impedance network, respectively; u_{pv} is the output voltage of the PV system; and i_{inv} is the equivalent current flowing into the H-bridge. In steady state, the following relationships between the Z-source inductor and PV currents and between the Z-source capacitor and PV voltages are

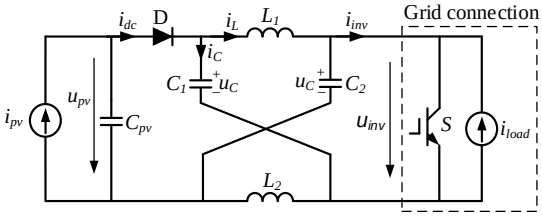

(a) Equivalent dc-side circuit of the ZSI connected to PV

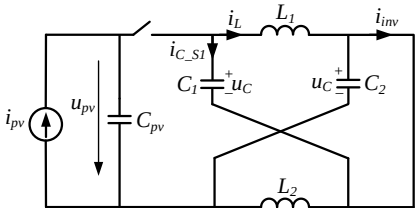

(b) Shoot-through state

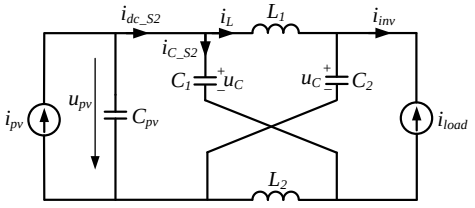

(c) Non shoot-through state

Fig. 2: The model at the dc side of the ZSI.

obtained from (1):

$$i_{pv} = i_L,$$
$$U_C = \frac{1 - D_{sh}}{1 - 2D_{sh}} U_{pv}. \quad (2)$$

Theoretically, the steady-state shoot-through duty ratio D_{sh} in (2) can vary from 0 to 0.5. In practice, it is limited by the zero-state interval T_0 of the ZSI [18, 19].

2.2 ac-side model

At the ac side of the ZSI, an LCL filter is employed to reduce the high-frequency current ripple, as shown in Fig. 3. However, the current controller only affects the low-order harmonics [20, 21]. Therefore, the LCL filter with a sufficiently small capacitator value can be replaced by an L filter L in series with its internal resistance r_L in the mathematical model to simplify the current controller design. The input voltage u_{inv} of the H-bridge is zero during the shoot-through state, while the value during the non-shoot-through state is [10]:

$$\hat{u}_{inv} = 2u_C - u_{pv} \quad (3)$$

The three-phase low-frequency average model of the ZSI at the ac side is as follows [22]:

$$L\frac{di_{sk}}{dt} = \hat{u}_{inv}\left(d_k - \frac{1}{3}\sum_{k=a,b,c} d_k\right) - e_{nk} - r_L i_{sk}, \quad (4)$$

where the subscript k represents phase a, b, and c, d_k is the corresponding PWM duty ratio, i_s is the ZSI output current (before the filter), and e_n is the ac-grid voltage. To facilitate the design of ac controllers, (4) is expressed in the synchronously rotating frame to decouple real and reactive power in the system as follows:

$$L\frac{di_{sd}}{dt} = \hat{u}_{inv}d_d - e_{nd} - r_L i_{sd} + \omega L i_{sd},$$
$$L\frac{di_{sq}}{dt} = \hat{u}_{inv}d_q - e_{nq} - r_L i_{sq} - \omega L i_{sq}, \quad (5)$$

where ω is the grid angular frequency; d_d, d_q are the d- and q-axis components of the PWM duty ratio, e_{nd} and e_{nq} are the d- and q-axis components of the grid voltage; and i_{sd}, i_{sq} are the d- and q-axis components of the grid current vector; $u_{sd} = \hat{u}_{inv}d_d$ and $u_{sq} = \hat{u}_{inv}d_q$ are the d- and q-axis components of the output voltage vector of the ZSI, respectively.

2.3 Switching models of the dc-side and ac-side

To conduct HIL real-time simulations, the switching functions of the impedance network s and of the IGBTs $s_k(k = a, b, c)$ are defined as follows [22]:

- s = 1 when the ZSI is in the shoot-through state.
- s = 0 when the ZSI is in the non-shoot-through state.
- s_k = 1 when the top switch of the phase leg is turned on and the bottom switch of the phase leg is turned off.
- s_k = 0 when the top switch of the phase leg is turned off and the bottom switch of the phase leg is turned on.

Using this definition and the average model in (1) and (4), the switched model of the ZSI is obtained as follows:

$$L\frac{di_L}{dt} = (2s - 1)u_C + (1 - s)u_{pv},$$
$$C\frac{du_C}{dt} = (1 - 2s)i_L + (s - 1)i_{inv},$$
$$C_{pv}\frac{du_{pv}}{dt} = i_{pv} - i_L,$$
$$L\frac{di_{sk}}{dt} = \hat{u}_{inv}\left(s_k - \frac{1}{3}\sum_{k=a,b,c} s_k\right) - e_{nk} - r_L i_{sk}. \quad (6)$$

3 Controller Design

The detailed control topology of the ZSI applied in the grid-tied PV systems in Fig. 1b is illustrated in Fig. 3. At the dc-side, the integrated MPPT and the proposed adaptive backstepping controller regulate PV output voltage u_{pv} and extract the maximum power from the PV panel. The Incremental Conductance MPPT method is used since it is easily implemented and exhibits fast convergence speed [23]. At the ac side, conventional PI and dead-beat controllers regulate the Z-source capacitor voltage u_C and the power factor.

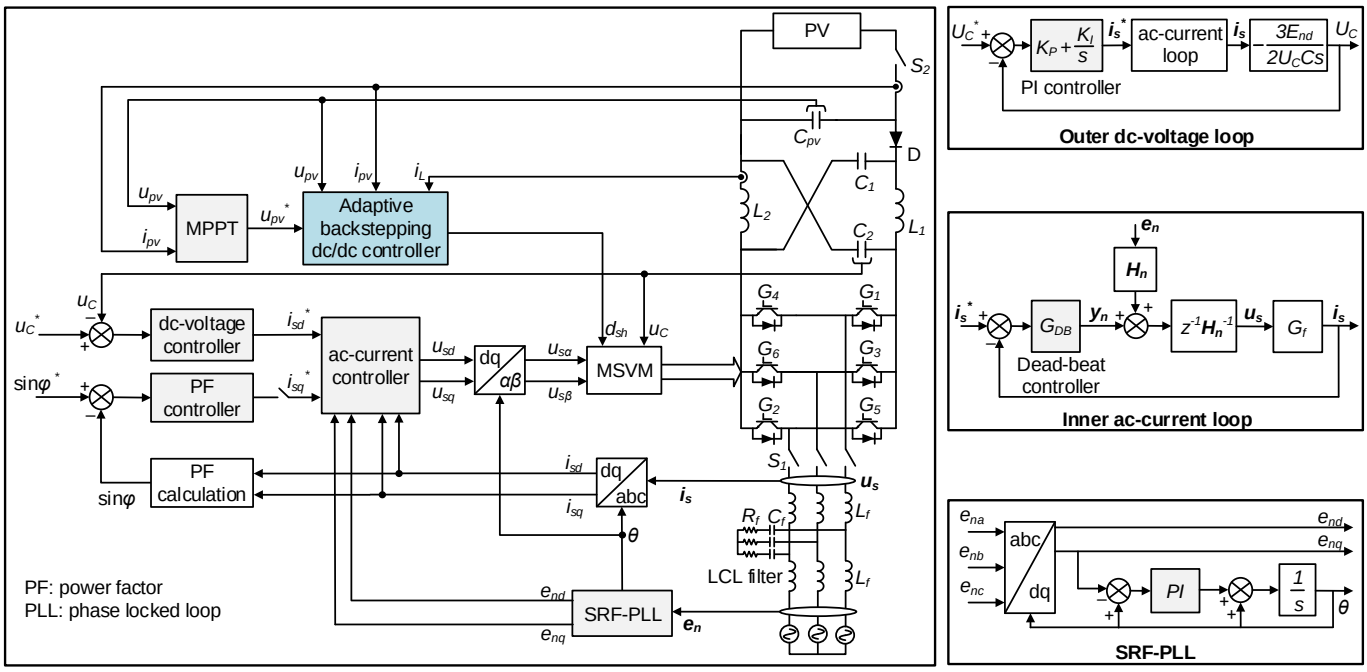

Fig. 3: The proposed multi-loop control for the ZSI in grid-tied PV systems.

3.1 The proposed dc-side adaptive backstepping controller

During normal operation of the ZSI in grid-tied PV systems, the values of inductors and capacitors in the impedance network deviate from the nominal values. This may impair the performance of conventional PI controllers, which are designed using the nominal component values. To solve this problem, the proposed adaptive backstepping controller employs a certainty-equivalence form in which unknown parameters are replaced by estimated parameters [24]. The controller design is based on the dc state-space model without any linearisation required as in conventional PI design approaches.

Assuming the Z-source capacitor voltage u_C is kept constant by the ac-side controllers, the dynamic dc-side model shown in (1) is rewritten in a state-space form as follows:

$$\begin{cases} \dot{x}_1 &= \theta_L[(1-d_{sh})x_2 + (2d_{sh}-1)u_C], \\ \dot{x}_2 &= \theta_C(i_{pv} - x_1), \end{cases} \tag{7}$$

where the state variable $\boldsymbol{x}^T = [x_1\ x_2]^T = [i_L\ u_{pv}]^T$, θ_L = 1/L, and θ_C= 1/C_{pv}. The purpose of the adaptive backstepping controller is to compute the shoot-through duty ratio d_{sh} to globally stabilize the PV voltage $x_2 = u_{pv}$ in (7) to a desired equilibrium point u^*_{pv}, which is given by the MPPT algorithm. The global stability is proved by using properly defined Lyapunov functions [24]. The detailed step-by-step adaptive backstepping design for system (7) is described as follows.

Step 1: Consider state x_1 as a virtual control input of the system (7). Define the error between state x_2 and its reference value u^*_{pv}, which is the output of the MPPT algorithm, as follows:

$$z_1 = x_2 - u^*_{pv}. \tag{8}$$

Differentiating z_1 with respect to time gives:

$$\begin{aligned} \dot{z}_1 &= \theta_C(i_{pv} - x_1) - \dot{u}^*_{pv} \\ &= (\hat{\theta}_C + \tilde{\theta}_C)(i_{pv} - x_1) - \dot{u}^*_{pv}, \end{aligned} \tag{9}$$

where $\hat{\theta}_C$ is the estimated value of θ and $\tilde{\theta}_C$ is the estimated error. Based on the definition of Lyapunov functions in [24], the first Lyapunov function candidate is chosen as follows:

$$V_1 = \frac{1}{2}z_1^2 + \frac{1}{2\gamma_C}\tilde{\theta}_C^2, \tag{10}$$

where γ_C is a positive adaptation gain. It is clear that V_1 is positive definite. The derivative of V_1 with respect to time is:

$$\begin{aligned} \dot{V}_1 &= z_1\dot{z}_1 + \frac{1}{\gamma_C}\tilde{\theta}_C\dot{\tilde{\theta}}_C \\ &= -k_1 z_1^2 + z_1(k_1 z_1 + \dot{z}_1) + \frac{1}{\gamma_C}\tilde{\theta}_C\dot{\tilde{\theta}}_C \\ &= -k_1 z_1^2 + z_1\{k_1 z_1 + [\hat{\theta}_C(i_{pv} - x_1) - \dot{u}^*_{pv}]\} + \\ &\quad + \tilde{\theta}_C\left[\frac{\dot{\tilde{\theta}}_C}{\gamma_C} + z_1(i_{pv} - x_1)\right], \end{aligned} \tag{11}$$

where k_1 is a positive design parameter providing necessary damping for system stabilization (7). In order to achieve global stability, $\dot{V}_1$ must be negative definite. Therefore, x_1 can be chosen as follows:

$$x_1 = \frac{k_1 z_1 - \dot{u}^*_{pv}}{\hat{\theta}_C} + i_{pv}. \tag{12}$$

The last term of $\dot{V}_1$ in (11) is eliminated by using the updated rule (13) and observing that θ_C is constant:

$$\dot{\hat{\theta}}_C = \gamma_C z_1(i_{pv} - x_1). \tag{13}$$

Substituting the expression in (13) and (12) into (11) yields:

$$\dot{V}_1 = -k_1 z_1^2 < 0 \tag{14}$$

Equation (14) shows that the positive-definite function V_1 chosen from (10) is a Lyapunov function. Therefore, x_2 is globally stable if the virtual control input x_1 mimics the behavior of the following stabilizing function, which is defined based on (12):

$$\alpha_1(u^*_{pv}, i_{pv}) = \frac{k_1 z_1 - \dot{u}^*_{pv}}{\hat{\theta}_C} + i_{pv}. \tag{15}$$

Step 2: Define the second error variable z_2 as the error between x_1 and the stabilizing function α_1:

$$z_2 = x_1 - \alpha_1. \tag{16}$$

Substituting the expressions (15) and (16) into (9) yields:

$$\dot{z}_1 = -\hat{\theta}_C z_2 - k_1 z_1 + \tilde{\theta}_C(i_{pv} - x_1). \tag{17}$$

From (7), (15), and (16), the derivative of z_2 with respect to time is given by:

$$\begin{aligned} \dot{z}_2 &= \theta_L[(2d_{sh}-1)u_C + (1-d_{sh})x_2] \\ &\quad - \frac{(k_1\dot{z}_1 - \ddot{u}^*_{pv})\hat{\theta}_C - \gamma_C z_1(i_{pv} - x_1)(k_1 z_1 - \dot{u}^*_{pv})}{\hat{\theta}_C^2} - \dot{i}_{pv}. \end{aligned} \tag{18}$$

The new model of the system shown in (17) and (18) is expressed in the coordinates (z_1, z_2), and a state-feedback control law is designed to globally and asymptotically stabilize (GAS) the system at the equilibrium point (z_1, z_2) = (0, 0). The second Lyapunov function candidate is chosen as follows:

$$V_2 = \frac{1}{2}z_1^2 + \frac{1}{2}z_2^2 + \frac{1}{2\gamma_C}\tilde{\theta}_C^2 + \frac{1}{2\gamma_L}\tilde{\theta}_L^2, \tag{19}$$

where the parameter error $\tilde{\theta}_L = \theta_L - \hat{\theta}_L$ and γ_L is the second positive adaptation gain. From (19), it is clear that V_2 is positive definite. The derivative of V_2 with respect to time is obtained as follows:

$$\begin{aligned} \dot{V}_2 &= z_1\dot{z}_1 + z_2\dot{z}_2 + \frac{1}{\gamma_C}\tilde{\theta}_C\dot{\tilde{\theta}}_C + \frac{1}{\gamma_L}\tilde{\theta}_L\dot{\tilde{\theta}}_L \\ &= -k_1 z_1^2 - k_2 z_2^2 + z_2\Bigg(\hat{\theta}_L[(2d_{sh}-1)u_C + (1-d_{sh})x_2] \\ &\quad - \frac{(k_1\dot{z}_1 - \ddot{u}^*_{pv})\hat{\theta}_C - \dot{\hat{\theta}}_C(k_1 z_1 - \dot{u}^*_{pv})}{\hat{\theta}_C^2} - i^*_{pv} + k_2 z_2 - \hat{\theta}_C z_1\Bigg) \\ &\quad + \tilde{\theta}_C\left[\frac{\dot{\tilde{\theta}}_C}{\gamma_C} + z_1(i_{pv} - x_1)\right] \\ &\quad + \tilde{\theta}_L\left\{\frac{\dot{\tilde{\theta}}_L}{\gamma_L} + z_2[(2d_{sh}-1)u_C + (1-d_{sh})x_2]\right\}, \end{aligned} \tag{20}$$

where k_2 is another positive design parameter. $\tilde{\theta}_C$ and $\tilde{\theta}_L$ are eliminated from $\dot{V}_2$ with the updated law (21):

$$\begin{cases} \dot{\hat{\theta}}_C = -\dot{\tilde{\theta}}_C = \gamma_C z_1(i_{pv} - x_1), \\ \dot{\hat{\theta}}_C = -\dot{\tilde{\theta}}_L = \gamma_L z_2[(2d_{sh}-1)u_C + (1-d_{sh})x_2], \end{cases} \tag{21}$$

where the shoot-through duty ratio, which is the actual control input of the system (7), is calculated as:

$$d_{sh} = \frac{1}{\hat{\theta}_L(2u_C - x_2)} \times \times \left[\frac{(k_1\dot{z_1} - \ddot{u}^*_{pv})\hat{\theta}_C - \gamma_C z_1(i_{pv} - x_1)(k_1 z_1 - \dot{u}^*_{pv})}{\hat{\theta}^2_C} + \right. \left. + \dot{i}_{pv} - k_2 z_2 + \hat{\theta}_c z_1 - \hat{\theta}_L(x_2 - u_C) \right]. \quad (22)$$

Substituting (21) and (22) into (17) and (18) yields:

$$\begin{cases} \dot{z}_1 = -\hat{\theta}_C z_2 - k_1 z_1 + \tilde{\theta}_C(i_{pv} - x_1), \\ \dot{z}_2 = \hat{\theta}_C z_1 - k_2 z_2 + \tilde{\theta}_L[(2d_{sh} - 1)u_C + (1 - d_{sh})x_2]. \end{cases} \quad (23)$$

Substituting (21) and (22) into (20) yields :

$$\dot{V}_2 = -k_1 z_1^2 - k_2 z_2^2 \leq 0. \quad (24)$$

Therefore, the positive-definite function V_2 chosen from (19) is also a Lyapunov function. Equation (23) implies that $(z_1, z_2) = (0, 0)$ and $(\tilde{\theta}_C, \tilde{\theta}_L) = (0, 0)$ are two equilibrium points of the closed-loop adaptive system, and (24) shows that the control error (z_1, z_2) = (0, 0) is GAS. Based on the definition of z_1 from (9), $x_2(t) \to u^*_{pv}$ as $t \to \infty$, i.e. the proposed adaptive backstepping controller using the control signal d_{sh} (22) globally stabilizes the PV voltage u_{pv} to its reference value u^*_{pv}. The values of k_1, k_2, γ_L, and γ_C of the dc-side controller using the backstepping method will be chosen based on simulation results.

3.2 The ac-side controllers

This section briefly describes the ac-side controllers, which are well established in the literature, based on the ac-side model shown in Section 2.2. As shown in Fig. 3, the double-loop control topology at the ac side consists of a slow outer dc-voltage loop and a fast inner ac-current loop. The output of the dc-voltage and power factor controllers provide the reference i_{sd} and i_{sq} for the ac-current loop. The output u_{sd} and u_{sq} of the ac-current controller are transformed to u_α and u_β before being sent to the modified space vector modulation (MSVM) algorithm to generate the switching signals for the IGBTs. To minimize the voltage stress across the inverter switches, the shoot-through time in this paper is evenly assigned to each phase with T_{sh}/6, while the active state times are not changed. With this strategy, the shoot-through time is limited to 3/4 of the zero-state interval T_0 [18, 19].

The outer dc-voltage loop is responsible for regulating the capacitor voltage u_C across capacitors C_1 and C_2 in the impedance network. The dc-voltage controller is designed as a conventional PI controller in the s domain.

The inner ac-current loop implicitly regulates the power factor of the system by controlling $dq-$components i_{sd} and i_{sq} of the ZSI output current $\boldsymbol{i_s}$. In this paper, i_{sq} is set to zero so that the system operates with unity power factor. To improve the dynamic response of the system, especially during transient conditions such as voltage sag or generated power variation, the ac-current controller is designed as a deadbeat controller in the discrete domain z instead of a conventional PI controller. The ac-current loop is also shown in Fig. 3 [25].

The performance of the controllers at the ac side relies heavily on the measurement of the phase angle of the grid voltage $\boldsymbol{e_n}$. This angular measurement requires accurate and robust acquisition when the grid voltage waveform is distorted and unbalanced. In this paper, the synchronous reference frame phase locked loop (SRF-PLL) method is implemented [20]. SRF-PLL translates the three-phase voltage vector from the abc reference frame to the dq synchronously rotating frame by using Park's transformations. A feedback loop regulates the q component of the grid voltage e_{nq} to zero, which results in the angular position of the dq rframe being locked into the phase angle of the grid voltage.

4 Off-line and real time simulation results

4.1 Case studies

To demonstrate the effectiveness of the proposed controller, a ZSI in a grid-tied PV system is simulated under different operating conditions using Simpower Systems Toolbox in Matlab/Simulink. A second validation is performed by means of HIL analysis using a digital signal processor (DSP). The parameters of the system under consideration are listed in Table 1. The range of PV voltage U_{pv} and set point of U_C are chosen such that the shoot-through ratio is limited to 0.4. It guarantees the input dc voltage of the H-bridge to be less than 5 times of the input PV voltage.

The PV module used in this simulation is SQ160/Shell [26]. The PV array is composed of 8 modules connected in series and 10 modules connected in parallel. All modules are considered to be identical and work in similar conditions of temperature T and irradiance G. Based on the datasheet from the manufacturer [26], the voltage and current of PV arrays at the maximum power points (MPP) under different working conditions are calculated as shown in Table 2. The working temperature is either 25 ^{o}C or 50 ^{o}C, while the working irradiance is either 500 W/m^2 or 1000 W/m^2.

The sequence of operating the system is as follows:

- The control system is initially disabled, and the switches S_1 and S_2 in Fig. 3 remain open.
- After switch S_1 is closed, the PLL block and the ac-side control are enabled to regulate the voltage U_C across the capacitors C_1 and C_2 at the desired value.

Table 1 System parameters.

Quantities	Values
Grid voltage	380 V / 50 Hz
Set point of U_C	570 Vdc
Range of PV voltage U_{pv}	190-348 Vdc
Parameters of the Z-source network	$C_1 = C_2 = 235\ \mu$F $\pm$ 10 % $L_1 = L_2 = 1.4$ mH $\pm$ 20 %
PV capacitor	$C_{pv} = 470\ \mu$F $\pm$ 10 %
Grid inductor	$L_s = 2$ mH
Parameters of the backstepping method	$k_1 = 5000$ $k_2 = 2000$
Adaptation gain	$\gamma_L = 0.1$ $\gamma_C = 0.5$
Parameters of the capacitor-voltage controller	$\zeta = 1.1$ $\omega_n = 60$ Hz
Switching frequency	5 kHz
Sample time of the ac-current controller	$T_s = 200\ \mu$s
Sample time of the MPPT algorithm and capacitor-voltage controller	1 ms

Table 2 MPP of the PV array under different working conditions [26].

Working condition	Voltage and current at the MPP
T = 25^{o}C, G = 500 W/m^2	V = 280 V, I = 23 A
T = 25^{o}C, G = 1000 W/m^2	V = 280 V, I = 45.8 A
T = 50^{o}C, G = 1000 W/m^2	V = 248 V, I = 45.8 A

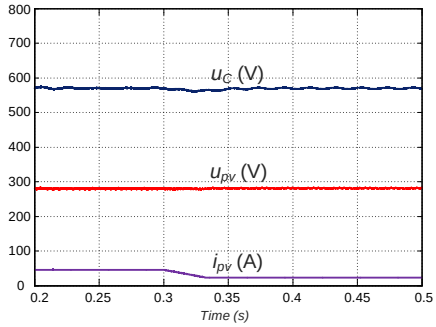

(a) PV output voltage and current and voltage across the Z-source impedance capacitor.

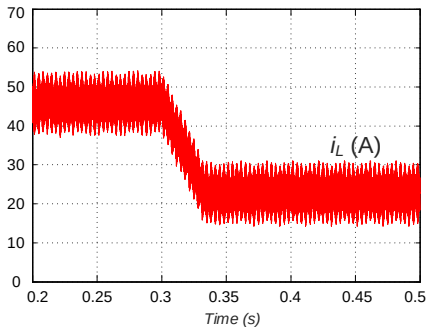

(b) Inductor current.

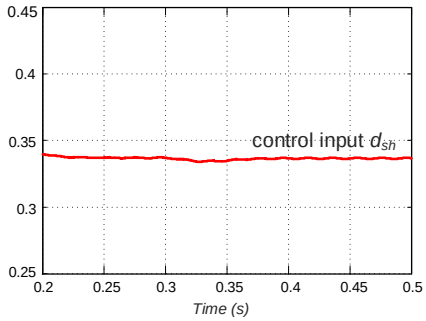

(c) Shoot-through duty ratio.

Fig. 4: The simulation results of the system when G decreases from 1000 W/m^2 to 500 W/m^2 at t = 0.3s, T = 25^{o}C.

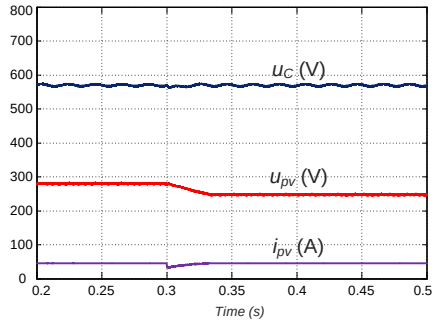

(a) PV output voltage and current and voltage across the Z-source impedance capacitor.

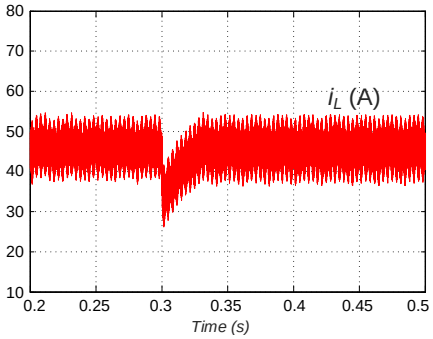

(b) Inductor current.

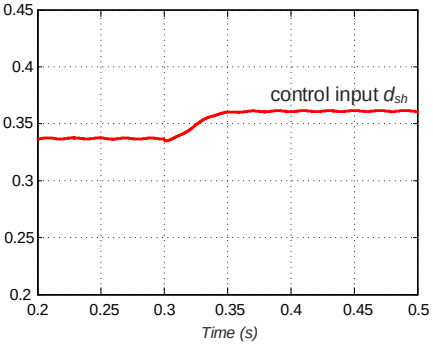

(c) Shoot-through duty ratio.

Fig. 5: The simulation results of the system when T changes from 50^{o}C to 25^{o}C at t = 0.3s, G = 1000 W/m^2.

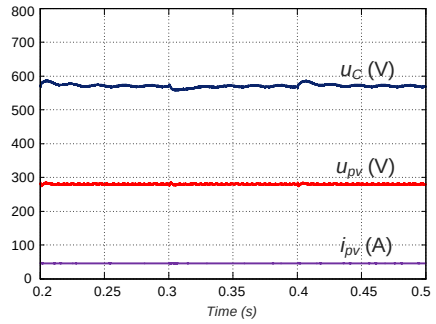

(a) PV output voltage and current and voltage across the Z-source impedance capacitor.

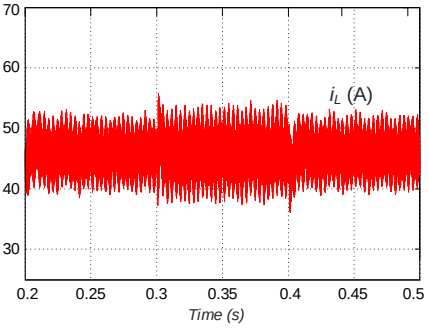

(b) Inductor current.

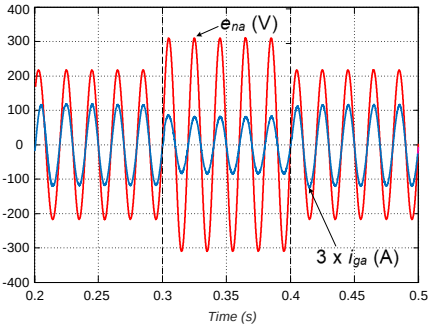

(c) Phase A grid voltage and current.

Fig. 6: The simulation results of the system when the grid voltage varies between 1 pu and 0.7 pu at t = 0.3s and at t = 0.4s.

• Finally, switch S_2 is closed, and the MPPT algorithm as well as the dc-side control are enabled. The power generated by the solar panels increases until the MPP is reached.

4.2 The off-line simulation results

The off-line simulations are carried out with the variations in solar irradiance, temperature, and ac grid voltage. In addition, the robustness of the proposed adaptive backstepping control is also demonstrated by linearly increasing the values of L_1 and L_2 from 1.12 mH to 1.68 mH (1.4 mH $\pm$ 20%), C_1 and C_2 from 211 μF to 258.5 μF (235 μF $\pm$ 10%), and C_{pv} from 423 μF to 517 μF (470 μF $\pm$ 10%), during the 0.5 seconds simulation time.

Fig. 4 shows the simulation results when the solar irradiance drops suddenly from 1000 W/m^2 to 500 W/m^2 at t = 0.3 s, while the temperature and the voltage across the Z-source impedance capacitor are constant at 25 ^{o}C and 570 V, respectively. The PV voltage and current in Fig. 4a closely match the theoretical values at the maximum power points (280 V, 45.8 A) and (280 V, 23 A), as shown in Table 2. With the proposed adaptive backstepping method, the PV voltage and current seamlessly follow the optimal values without any significant overshoots or undershoots, compared to [9, 14]. The ac-side controllers of the reconfigured control scheme also maintain the voltage across the capacitors in the impedance network at the desired value of 570 V (from Table 1). Fig. 4b shows that the inductor current transitions smoothly between two steady-state values of irradiance. The steady-state value D_{sh} of the shoot-through ratio is calculated as follows:

$$D_{sh} = \frac{U_C - U_{pv}}{2U_C - U_{pv}} = \frac{570 - 280}{2 \times 570 - 280} = 0.3372, \qquad (25)$$

which is consistent with the shoot-through duty ratio shown in Fig. 4c. When the solar irradiance drops further, the shoot-through duty ratio does not change significantly, and both the dc and ac controllers are still able to maintain PV voltage U_{pv} and Z-source capacitor voltage U_C at 280 V and 570 V, respectively.

Fig. 5 shows the simulation results when the temperature drops from 50°C to 25°C at t = 0.3 s, while irradiance is constant at 1000 W/m^2. The adaptive backstepping controller at the dc side regulates the PV voltage and current in Fig. 5a to track the theoretical values at the maximum power points (280 V, 45.8 A) and (248 V, 45.8 A), as shown in Table 2. The ac-side controllers maintain the voltage across capacitors C_1 and C_2 at the desired value of 570 V. No overshoot is observed compared to [9, 14]. Fig. 5b shows the inductor current with an acceptable transition between the two steady-state values of temperature. Similar to (25), the steady-state values of the shoot-through ratio D_{sh} at the two maximum power points are calculated to be D_{sh1} = 0.3372 and D_{sh2} = 0.3610. These values are consistent with the results in Fig. 5c. From (2), since the output voltage of the PV array decreases, D_{sh} increases to keep the Z-source voltage across the capacitors in the impedance network constant.

Fig. 6 shows the simulation results when the grid voltage steps up and down between 1 p.u and 0.7 p.u (220 Vrms and 154 Vrms, respectively). The temperature and irradiance are constant at 25°C and 1000 W/m^2, respectively. As shown in Fig. 6a, the output voltage and current of the PV array are not affected by the ac grid voltage variation, and their steady-state values are close to the theoretical values at the maximum power points (280 V, 45.8 A), as shown in Table 2. With the implementation of the capacitor voltage controller at the ac side (Fig. 1b), the voltage across the capacitors in the impedance network is kept close to the desired value in spite of the grid voltage fluctuation. No significant overshoot in the waveform of the capacitor voltage is observed. Fig. 6b shows the inductor current with very small overshoots during transient periods. Since the power transferred from the PV array does not change, the current injected into the ac grid increases when the grid voltage decreases, as shown in Fig. 6c. The total harmonic distortion of the ZSI output current obtained using the FFT toolbox of MATLAB/POWERGUI is equal to 4.63%. The grid current and voltage at the ac side of the ZSI are distortion-free. They remain sinusoidal and in-phase throughout the simulation because the inverter is regulated to operate at unity power factor. It should be noted that the response time of the system in all three cases in Fig. 4 - Fig. 6 is less than 0.05 second.

Similar operating conditions to those in Fig. 4 and Fig. 5, in which the irradiance and temperature suddenly vary at t = 0.3 s, are applied for the simulated system employing the control topology in Fig. 1b with linear controllers at the dc side. The proposed nonlinear adaptive backstepping controller is replaced by a multi-loop control scheme using PI and P controllers for the outer voltage-control loop and the inner current-control loop, respectively. The parameters of the PI and P controllers are determined based on the operating points corresponding to the initial conditions of irradiance G and temperature T before 0.3 s. The simulation results of the PV voltage and current and the inductor current in the impedance network are shown in Fig. 7. It is clear that the PV voltage and current as well as the inductor current are unstable following a variation of either irradiance G or temperature T. To maintain system stability at the new operating point, the parameters of the PI and P controllers need to be modified properly.

These simulation results validate the capability and advantages of the proposed adaptive backstepping method at the dc side as well as the reconfigured control topology in Fig. 1b in terms of stabilizing the PV and Z-source capacitor voltages under different operating conditions and variations of both the PV and ac grid.

4.3 HIL real-time simulation results

In this section, HIL real-time simulation is carried out to verify the performance of the proposed adaptive backstepping controller and the reconfigured multi-loop control scheme in Fig. 1b. HIL simulation has been shown to be an effective design approach with its ease in adjusting PV real-time operating parameters, modifying controller

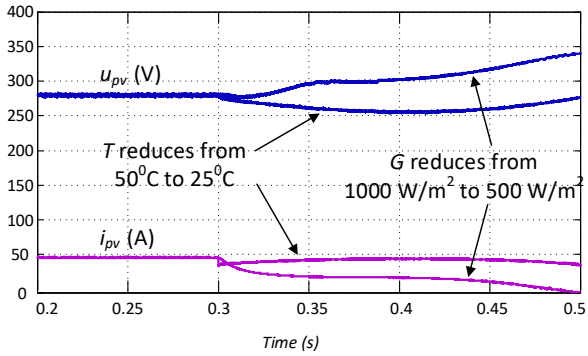

(a) PV output voltage and current.

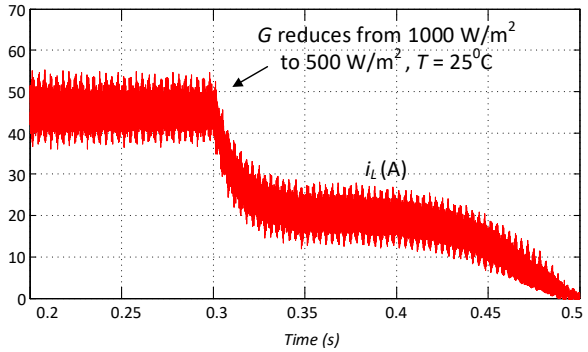

(b) Inductor current with a variation of irradiance G.

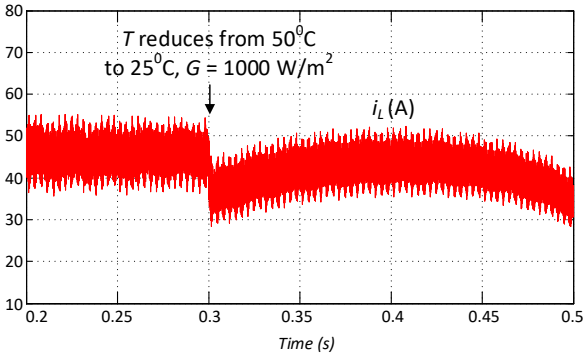

(c) Inductor current with a variation of temperature T.

Fig. 7: The simulation results of the system employing the control topology in Fig. 1b with linear controllers at both ac and dc sides.

parameters, and analyzing system dynamic response. In addition, HIL simulation greatly reduces simulation time and cost. The disadvantage of HIL simulation is that it considers switching devices and passive components such as capacitors and inductors as ideal elements [27].

The experimental HIL setup is shown in Fig. 8. The switched model of the ZSI obtained from Section 2.3 is loaded on the dSPACE DS1103 PPC controller board and Matlab's Real-Time Workshop (now Simulink Coder) toolbox. A high operating frequency of the switched model results in a better representation of the real system. In this study, this frequency is limited by the clock frequency of the DS1103 board, which is 100 kHz. The controllers are implemented in the fixed-point 32-bit type TMS320F2812 DSP by Texas Instruments. The switching pulses are generated from the PWM channel of the DSP and sent to the digital input-output interface with the DS1103 board. The measured signals of the grid-tied PV system are sent to the DAC channels of the DS1103 board and the ADC channels of the DSP.

The execution time of the simulation model should be at least 10-20 times lower than the switching period to achieve real-time

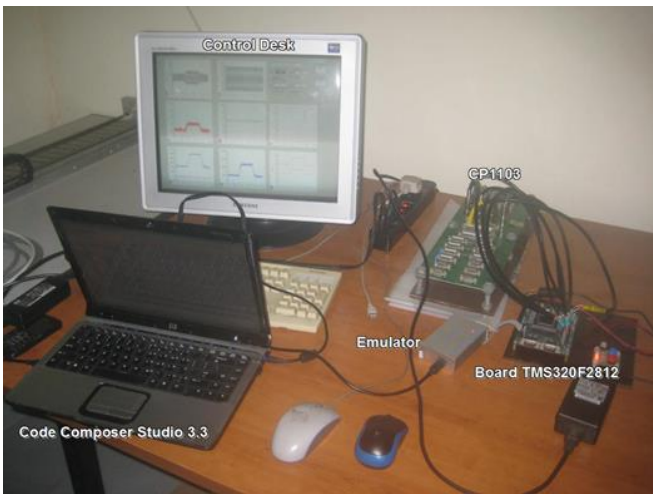

Fig. 8: Experimental HIL setup.

operation. In this paper, the execution time is set at 10 μs and the PWM switching frequency is 5 kHz. All variables used by the Simulink model are accessed by using the ControlDesk package. The temperature and irradiance of the PV array can be changed on-line to test the robustness of the control algorithm.

For the digital implementation, the derivative components in (22) can be discretized as follows:

$$\begin{cases} \dfrac{dy}{dt} & = \dfrac{y(k)-y(k-1)}{T_s}, \\ \dfrac{d^2y}{dt^2} & = \dfrac{y(k)-2y(k-1)+y(k-2)}{T_s^2} \end{cases} \tag{26}$$

The first case study analyzes the working condition corresponding to Fig. 4. The irradiance of the PV array is decreased from 1000 W/m^2 to 500 W/m^2 and increased again to 1000 W/m^2, while the temperature of the PV array is kept at 25^{o}C. The rms value of the line-to-neutral grid voltage is 220 V. Fig. 9 shows the HIL results recorded by the virtual scopes. The output voltage of the PV array and the voltage across the Z-source impedance capacitor are stably held at 280 V and 570 V, respectively, without any significant overshoots, as shown in Fig. 9a and 9b. The Z-source inductor current and the ZSI output current at the grid side are shown in Fig. 9c and 9d, respectively. The average steady-state values of the Z-source inductor current are 45.8 A and 23 A, which is consistent with Fig. 4b. The PV output current, which is not shown here due to limited space, is equal to the Z-source inductor current. Therefore, comparing these results with the theoretical data in Table 2 proves that the ZSI in the grid-tied PV system transfers the maximum power generated from the PV array to the ac grid.

In the second case study related to Fig. 5, the temperature of the PV array is changed from 50^{o}C to 25^{o}C and then returned to 50^{o}C, while the irradiance of PV array is kept at 1000 W/m^2. The rms value of the line-to-neutral grid voltage is 220 V. The results are shown in Fig. 10. Similar to the results shown in Fig. 5, the output voltage of the PV array and the voltage across the Z-source impedance capacitor in Fig. 10a and Fig. 10b are stable at 570 V and 280 V, respectively. The Z-source inductor current and the ZSI output current at the grid side are shown in Fig. 10c and Fig. 10d. The Z-source inductor current and the PV output current, which is not shown, approximates 45.8 A, which is the theoretical value at the maximum power point under these operating conditions. Therefore, the proposed control for the ZSI also allows the maximum power generated from the PV array to be delivered to the ac grid in this second case study.

In both off-line and HIL experiments, the capacitor voltage ripple and inductor current ripple are less than 5% and 20%, which is acceptable for practical applications [28]. These ripples would reduce with larger capacitors and inductors; however, the system response would be slower.

5 Conclusion

This paper proposes an adaptive backstepping control at the dc side of a reconfigured multi-loop control scheme for applications of the

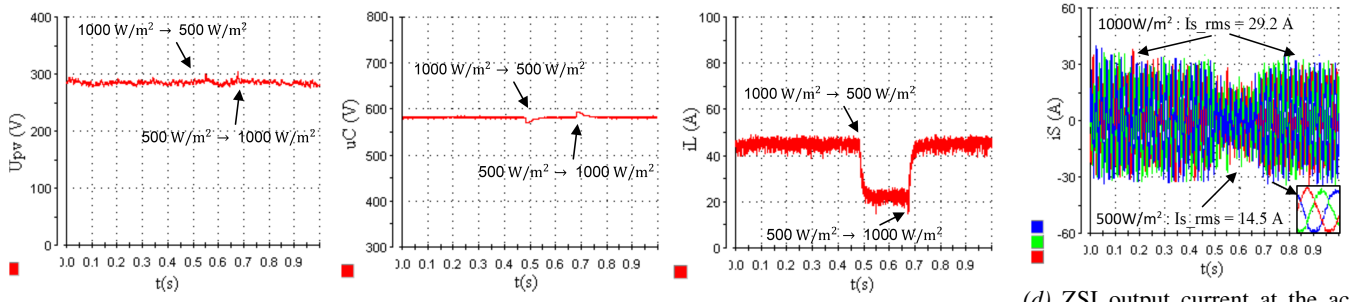

(a) PV array output voltage. *(b)* Z-source capacitor voltage. *(c)* Z-source inductor current. *(d)* ZSI output current at the ac side.

Fig. 9: Real-time simulation results when G changes from 1000 W/m^2 to 500 W/m^2, T = 25^{o}C.

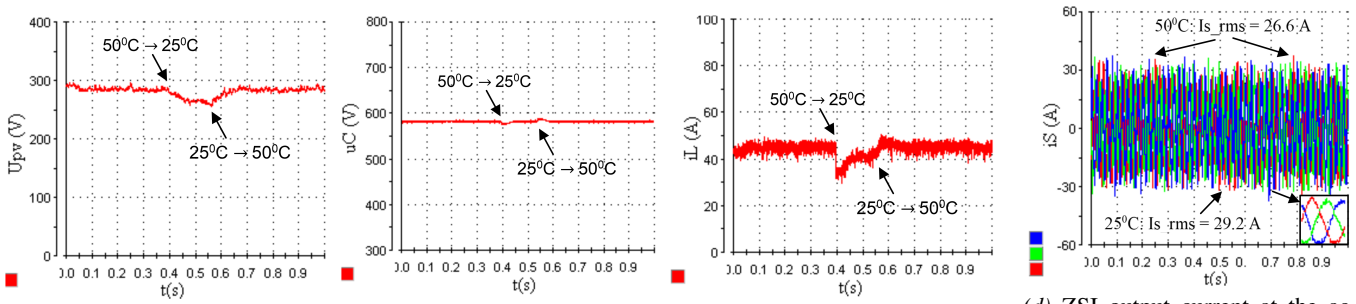

(a) PV array output voltage. *(b)* Z-source capacitor voltage. *(c)* Z-source inductor current. *(d)* ZSI output current at the ac side.

Fig. 10: Real-time simulation results when T changes from 50^{o}C to 25^{o}C, G = 1000 W/m^2.

ZSI in grid-tied PV systems. The proposed adaptive backstepping method eliminates the need to linearise the voltage/current characteristics of PV arrays and the ZSI model as in conventional approaches. It also takes into account the uncertainty of inductor and capacitor values in the impedance network. The stability of the system with the adaptive backstepping controller is proven by applying the Lyapunov method. The voltage across the capacitors in the impedance network is regulated by the ac side controllers. Off-line and HIL real-time simulations verify the robustness of the proposed control method in maintaining system stability and significantly reducing overshoot in the waveform of PV and Z-source capacitor voltages under varying conditions of irradiance, temperature, and ac grid voltage amplitude. In addition, in spite of the clock-frequency limitation when emulating the real system, the HIL provides another effective approach in terms of cost and safety for designing and verifying power electronics controllers. With the increasing PV penetration in distribution systems, the proposed control approach facilitates the deployment of Z-source inverters in practical applications to deal with the wide operating ranges of both power and voltage from PV arrays.

6 Acknowledgment

The experimental system in this paper was supported by the Institute for Control Engineering and Automation (ICEA) at Hanoi University of Science and Technology (HUST).

7 References

1 Y. Liu, H. Abu-Rub, B. Ge, F. Blaabjerg, O. Ellabban, and P. C. Loh, *Impedance Source Power Electronic Converters,*. Hoboken, NJ: John Wiley & Sons Ltd., 2016.
2 F. Z. Peng, "Z-source inverter," *IEEE Transactions on Industry Applications*, vol. 39, no. 2, pp. 504–510, March 2003.
3 Y. Huang, M. Shen, F. Z. Peng, and J. Wang, "Z-source inverter for residential photovoltaic systems," *IEEE Transactions on Power Electronics*, vol. 21, no. 6, pp. 1776–1782, Nov 2006.
4 X. Chen, Q. Fu, D. Infield, and S. Yu, "Modeling and control of Z-source grid-connected PV system with APF function," in *2009 44th International Universities Power Engineering Conference (UPEC)*, Sept 2009, pp. 1–5.
5 J. Liu, S. Jiang, D. Cao, X. Lu, and F. Z. Peng, "Sliding-mode control of quasi-Z-source inverter with battery for renewable energy system," in *2011 IEEE Energy Conversion Congress and Exposition*, Sept 2011, pp. 3665–3671.
6 X. Chen, Q. Fu, and D. G. Infield, "PV grid-connected power conditioning system with Z-source network," in *2009 International Conference on Sustainable Power Generation and Supply*, April 2009, pp. 1–6.
7 H. Abu-Rub, A. Iqbal, S. M. Ahmed, F. Z. Peng, Y. Li, and G. Baoming, "Quasi-Z-Source Inverter-Based Photovoltaic Generation System With Maximum Power Tracking Control Using ANFIS," *IEEE Transactions on Sustainable Energy*, vol. 4, no. 1, pp. 11–20, Jan 2013.
8 O. Ellabban and H. Abu-Rub, "Z-source inverter: Topology improvements review," *IEEE Industrial Electronics Magazine*, vol. 10, no. 1, pp. 6–24, March 2016.
9 C. J. Gajanayake, D. M. Vilathgamuwa, and P. C. Loh, "Development of a comprehensive model and a multiloop controller for Z-Source inverter DG systems," *IEEE Transactions on Industrial Electronics*, vol. 54, no. 4, pp. 2352–2359, August 2007.
10 O. Ellabban, J. V. Mierlo, and P. Lataire, "A DSP-Based Dual-Loop Peak DC-link Voltage Control Strategy of the Z-Source Inverter," *IEEE Transactions on Power Electronics*, vol. 27, no. 9, pp. 4088–4097, Sept 2012.
11 G. Ke, C. Yan, Z. Lin, and G. Yuanxing, "Research on the Z-source inverter grid-connected control of micro-grid based on differential geometry," in *Proceedings of the 2011 14th European Conference on Power Electronics and Applications*, Aug 2011, pp. 1–9.
12 Y. P. Siwakoti, F. Z. Peng, F. Blaabjerg, P. C. Loh, G. E. Town, and S. Yang, "Impedance-Source Networks for Electric Power Conversion Part II: Review of Control and Modulation Techniques," *IEEE Transactions on Power Electronics*, vol. 30, no. 4, pp. 1887–1906, April 2015.
13 G. Sen and M. E. Elbuluk, "Voltage and current-programmed modes in control of the Z-source converter," *IEEE Transactions on Industry Applications*, vol. 46, no. 2, pp. 680–686, March 2010.
14 C. J. Gajanayake, D. M. Vilathgamuwa, and P. C. Loh, "Small-signal and signal-flow-graph modeling of switched Z-source impedance network," *IEEE Power Electronics Letters*, vol. 3, no. 3, pp. 111–116, Sept 2005.
15 A. Zakipour, S. Shokri-Kojori, and M. Tavakoli Bina, "Sliding mode control of the nonminimum phase grid-connected Z-source inverter," *International Transactions on Electrical Energy Systems*, vol. 27, no. 11, pp. e2398–n/a, 2017, e2398 ITEES-17-0138.R1. [Online]. Available: http://dx.doi.org/10.1002/etep.2398
16 A. H. Rajaei, S. Kaboli, and A. Emadi, "Sliding-mode control of Z-source inverter," in *2008 34th Annual Conference of IEEE Industrial Electronics*, Nov 2008, pp. 947–952.
17 H. Rostami and D. A. Khaburi, "Neural networks controlling for both the DC boost and AC output voltage of Z-source inverter," in *2010 1st Power Electronic Drive Systems Technologies Conference (PEDSTC)*, Feb 2010, pp. 135–140.
18 Q. V. Tran, T. W. Chun, H. G. Kim, and E. C. Nho, "Minimization of voltage stress across switching devices in the Z-source inverter by capacitor voltage control," in *Journal of Power Electronics*, vol. 9, 2009, pp. 335–342.
19 Y. Liu, B. Ge, H. Abu-Rub, and F. Z. Peng, "Overview of space vector modulations for three-phase Z-Source/Quasi-Z-Source Inverters," *IEEE Transactions on Power Electronics*, vol. 29, no. 4, pp. 2098–2108, April 2014.
20 R. Teodorescu, M. Liserre, and P. Rodrguez, *Grid converters for photovoltaic and wind power systems*. John Wiley, Ltd, 2011.
21 M. Liserre, F. Blaabjerg, and S. Hansen, "Design and control of an LCL-filter-based three-phase active rectifier," *IEEE Transactions on Industry Applications*, vol. 41, no. 5, pp. 1281–1291, Sept 2005.
22 L. Jie, Q. Keqing, S. Xiaoliang, and C. Guo-cheng, "Study on control methods of direct-drive wind generation system based on three-phase Z-source inverter," in *2009 IEEE 6th International Power Electronics and Motion Control Conference*, May 2009, pp. 644–649.
23 T. Esram and P. L. Chapman, "Comparison of photovoltaic array maximum power point tracking techniques," *IEEE Transactions on Energy Conversion*, vol. 22, no. 2, pp. 439–449, June 2007.
24 M. Krstic, I. Kanellakopoulos, and P. Kokotovic, *Nonlinear and Adaptive Control Design*. John Wiley, Inc., New York., 1995.
25 Q. N. Phung and D. Jorg-Andreas, *Vector Control of Three-Phase AC Machines*. Springer, Berlin-Heidelberg, 2008.
26 Product information sheet, Sell-SQ160. [Online]. Available: http://www.oksolar.com/pv/shell.htm
27 R. Bojoi, F. Profumo, G. Griva, R. Teodorescu, and F. Blaabjerg, "Advanced research and education in electrical drives by using digital Real-Time Hardware-in-the-Loop simulation," in *Proceedings of Power Electronics and Motion Control Conference and Exposition (PEMC)*, 2002.
28 Texas Instruments, "Choosing inductors and capacitors for dc/dc converters," *Available at http://www.ti.com/lit/an/slva157/slva157.pdf*, Tech. Rep., 2014.